Dynamic Response of Ion Transport in Nanoconfined Electrolytes

Zengming Zhang[1], Chenkun Li[1], Jianbo Zhang[2], Michael Eikerling[1,3], Jun Huang[1,4*]

1 IEK-13, Institute of Energy and Climate Research, Forschungszentrum Jülich GmbH, 52425, Jülich, Germany

2 School of Vehicle and Mobility, State Key Laboratory of Automotive Safety and Energy, Tsinghua University, Beijing 100084, China

3 Chair of Theory and Computation of Energy Materials, Faculty of Georesources and Materials Engineering, RWTH Aachen University, 52062 Aachen, Germany

4 Theory of Electrocatalytic Interfaces, Faculty of Georesources and Materials Engineering, RWTH Aachen University, 52062 Aachen, Germany

** Corresponding author, e-mail: ju.huang@fz-juelich.de*

Abstract

Ion transport in nanoconfined electrolytes exhibits nonlinear effects caused by large driving forces and pronounced boundary effects. An improved understanding of these impacts is urgently needed to guide the design of key components of electrochemical energy systems. Herein, we employ a nonlinear Poisson-Nernst-Planck theory to describe ion transport in nanoconfined electrolytes coupled with two sets of boundary conditions to mimic different cell configurations in experiments. A peculiar nonmonotonic charging behavior is discovered when the electrolyte is placed between a blocking electrode and an electrolyte reservoir, while normal monotonic behaviors are seen when electrolyte is placed between two blocking electrodes. We reveal that impedance shapes depend on the definition of surface charge and the electrode potential. Particularly, an additional arc can emerge in the intermediate-frequency range at potentials away from the potential of zero charge. The obtained insights are instrumental to experimental characterization of ion transport in nanoconfined electrolytes.

Keywords: Ion transport, nanoconfinement, nonlinear Poisson-Nernst-Planck, solid electrolyte, impedance.

Ion transport is a fundamental process and sometimes the rate-determining step in electrochemical energy technologies, such as lithium-ion batteries. In the bulk phase, ion transport is often described using Fick's law with the ion flux being proportional to the concentration gradient (*1-4*). Near a charged interface, ion flux driven by the spatially varying electrical field cannot be neglected, and Poisson-Nernst-Planck (PNP) theory is often used in this context (*5-8*). Modified PNP theories have been developed for ion transport in concentrated solutions where the finite size of ions and short-range correlations between ions are important (*9-15*). In addition, dynamic density functional theory provides a unified framework to describe ion transport in complex fluids (*16-18*). In spite of the formal differences, these theories assume that the ion flux is linear with respect to the driving force, viz., the gradient of the electrochemical potential; different treatments lead to different expressions of the driving force and diffusion coefficient.

In general, the reaction flux is an exponential function of the driving force. One example is the Butler-Volmer equation for charge transfer at the interface between two phases. Ion transport could be viewed as a chain of ion-vacancy coupled charge transfer reactions (*19, 20*). This view leads to a Butler-Volmer-type equation for ion transport in which the ion flux is an exponential function of the electrochemical potential gradient of the examined ion, which was earlier developed by Riess and Maier (*21*). When the gradient of the electrochemical potential is small, the exponential function can be linearized and a PNP-type equation is retrieved (*22*). This linear approximation is valid for ion transport in bulk phase, as well as in thick electric double layers (EDL). However, one would expect it to become increasingly problematic when the length scale reduces to the order of Debye length, namely, when ion transport occurs in the presence of large electric fields, above 100 kV/cm (*23-27*).

In this paper, we study ion transport in electrolytes, be it solid or liquid, under nanoconfinement where the characteristic length is comparable to the Debye length. Under these conditions, nonlinear ion transport kinetics has been observed (*28-30*). A nonlinear PNP theory is employed for this purpose. To treat different boundary conditions found in practical systems, two types of cells, including single-blocking open cells (SBOC) and double-blocking closed cells (DBCC), are analyzed in detail in both time and frequency space. Though the models are simple and not new, several unexpected behaviors are observed, including nonmonotonic EDL charging behaviors in the time space for the SBOC, the dependency of impedance shape on the definition of the EDL charge, and an additional impedance arc at potentials deviating from the potential of zero charge (PZC) for the SBOC. The model for the DBCC case is further employed to interpret experimental impedance data of ion transport in solid electrolytes. We also briefly discuss the influence of charge transfer reactions on the results, leaving a detailed analysis for a future study.

We start with a one-dimensional model with an *ideally blocking* electrode and an electrolyte solution consisting of a binary symmetric electrolyte with ions of the same size. Within a primitive picture, the solvent is treated as a dielectric continuum with a constant permittivity ε_{S}. Considering the finite size of ions, we introduce a finite space between the electrode surface and the edge of the electrolyte phase, denoted the Helmholtz plane (HP), of which the permittivity $\varepsilon_{\mathrm{HP}}$ is much lower than ε_{S} (*31*). Nanoconfined electrolytes can have various boundary conditions in electrochemical energy devices. In metal-ion batteries, the solid-electrolyte interphase (SEI) can be mimicked as a nanoconfined electrolyte sandwiched between an electrode and a bulk electrolyte solution (*32-34*). Since the EDL can exchange particles with the electrolyte solution, we refer to it as a single-blocking open cell (SBOC), as illustrated in FIG 1. In measurements of the ion conductivity of solid electrolytes for solid-state batteries (*35-37*), the solid electrolyte is sandwiched between two blocking metals, and this case corresponds to a double-blocking closed cell (DBCC).

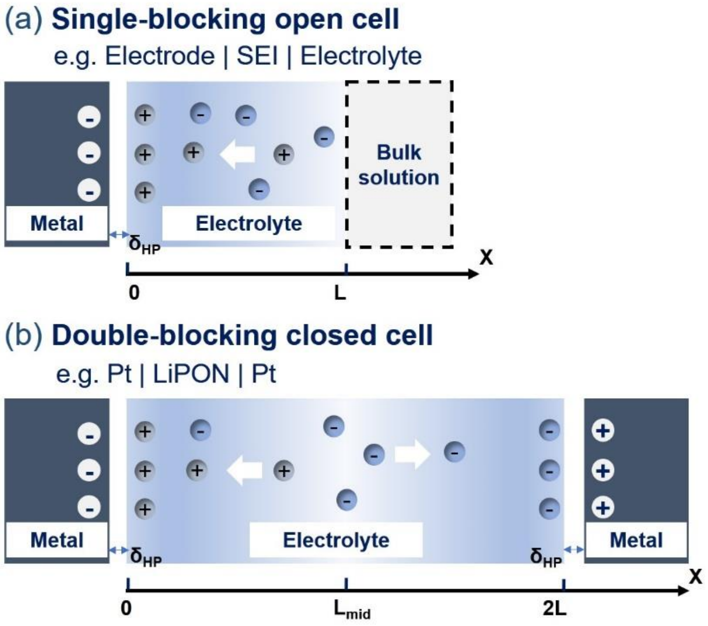

FIG 1. Schematic diagram of the two types of models. (a) Single-blocking open cell with one side in contact with a blocking electrode, and the other side connected to a reservoir of electrolyte solution; (b) Double-blocking closed cell with an electrolyte solution confined between two blocking electrodes. The solution consists of a binary symmetric electrolyte with ions of the same size.

Ion transport in nanoconfined electrolytes is described by a modified PNP theory (*20, 38*), which in the dimensionless form is given by,

$$\frac{\partial C_i}{\partial \tau} = \frac{\partial J_i}{\partial X}, \tag{1}$$

$$\frac{\partial^2 U}{\partial X^2} + \frac{(C_+ - C_-)}{2} = 0, \tag{2}$$

where C_i is the ion concentration referenced to the bulk concentration c_0^i, the subscript i representing cations (+) or anions (−), X is the spatial coordinate normalized by the Debye length $\lambda_D = \sqrt{\varepsilon_S RT/(2F^2 c_0)}$, $\tau = tD_+/{\lambda_D}^2$ is the dimensionless time, D_i is the diffusion coefficient of species i, $U = F\phi/RT$ is the dimensionless potential, other symbols have their usual meaning.

The flux term is given by (*19*),

$$J_{\pm} = \frac{D_{\pm}}{D_{+}} \cdot \frac{2\lambda_D}{a}\left(C_{\pm}(1-\gamma C)\right)\sinh\left[\frac{a}{2\lambda_D}\left(\frac{1}{C_{\pm}}\frac{\partial C_{\pm}}{\partial X} + \frac{\gamma}{(1-\gamma C)}\frac{\partial C}{\partial X} \pm \frac{\partial U}{\partial X}\right)\right], \tag{3}$$

with $\gamma = a^3 c_0 N_{\mathrm{A}}$ being the volume fraction of all ion in the bulk and $C = C_+ + C_-$ the total ion concentration. This nonlinear PNP equation can be reduced back to the linear PNP when the system remains in near-equilibrium, because $\sinh\zeta \approx \zeta$ for $\zeta \ll 1$: (*19, 20*),

$$J_{\pm} = \frac{D_{\pm}}{D_{+}}\left(C_{\pm}(1-\gamma C)\right)\left(\frac{1}{C_{\pm}}\frac{\partial C_{\pm}}{\partial X} + \frac{\gamma}{(1-\gamma C)}\frac{\partial C}{\partial X} \pm \frac{\partial U}{\partial X}\right). \tag{4}$$

At the left boundary, designated at the HP, $X = 0$, the flux vanishes for both SBOC and DBCC cases,

$$J_{\pm}(0,\tau) = 0. \tag{5}$$

As there is no extra charge in the space between the metal electrode surface and the HP, the potential distribution is linear in this region, (*39, 40*),

$$U(0,\tau) = U_{\mathrm{M}} + \frac{\delta_{\mathrm{HP}}}{\lambda_D}\frac{\varepsilon_{\mathrm{S}}}{\varepsilon_{\mathrm{HP}}}\frac{\partial U}{\partial X}(0,\tau), \tag{6}$$

where U_{M} is the surface potential applied on the left metal electrode.

The right boundary condition is contingent on the type of cell. For the SBOC, the nanoconfined electrolyte is connected with a constant-potential reservoir of electrolyte at $X = L$, namely,

$$C_+(L,\tau) = 1,\ C_-(L,\tau) = 1,\ U(L,\tau) = 0, \tag{7}$$

meaning that ion concentrations assume their bulk value and the electric potential serves as the reference.

For the DBCC, the right boundary at $X = 2L$ has a zero ion flux,

$$J_{\pm}(2L,\tau) = 0, \tag{8}$$

and the electrode potential satisfies,

$$U(2L,\tau) = -U_{\mathrm{M}} - \frac{\delta_{\mathrm{HP}}}{\lambda_D}\frac{\varepsilon_S}{\varepsilon_{\mathrm{HP}}}\frac{\partial U}{\partial X}(2L,\tau), \tag{9}$$

with $-U_{\mathrm{M}}$ being the applied potential on the right metal.

Before applying the potential perturbation, we find the electrolyte solution in uniform concentrations and zero electric potential for both SBOC and DBCC, namely,

$$C_+(X,0) = 1, C_-(X,0) = 1, U(X,0) = 0. \tag{10}$$

We employ the present model to explore the charging dynamics of nanoconfined electrolytes, described in terms of the EDL charge density as a function of time. Two definitions of EDL charge exist in the literature (*16, 41, 42*), as shown in FIG S1, including the total diffuse charge,

$$Q_{\mathrm{EDL}}(\tau) = \int_0^L \left(C_+(X,\tau) - C_-(X,\tau)\right) dX, \tag{11}$$

and the electrode surface charge,

$$Q_{\mathrm{M}}(\tau) = -\frac{\partial U(0,\tau)}{\partial X}. \tag{12}$$

These two charges are equivalent, if the electric field vanishes at $X = L$. Note that $Q_{\mathrm{M}}(\tau)$ does not start from zero, because the initial electric field at $X = 0$ has nonzero value, as shown in FIG S2. In the following, we use consistently the total diffuse charge $Q_{\mathrm{EDL}}(\tau)$ to describe the charging dynamics of the SBOC in FIG 2, and provide results in terms of $Q_{\mathrm{M}}(\tau)$ in FIG S3. The charging dynamics of EDL has been widely studied (*43-45*). Conventionally, it can be divided into a fast process with a time constant of $\tau_{\mathrm{RC}} = \lambda_D L/D_+$, and a slow process with a time constant of $\tau_D = L^2/D_+$ (*6, 40, 46, 47*). Such two-stage charging behaviors are observed for ‘thick’, namely, $L \gg \lambda_D$, electrolyte films, which are well described by the linear PNP theory. The charging dynamics of the DBCC given in FIG S4 (a) shows a similar charging behavior.

The nonlinear PNP theory differs from the linear PNP in two aspects. On the one hand, the nanoconfined electrolyte described using the nonlinear PNP theory charges faster, as shown in FIG 2(a), because the ion flux is larger under the same driving force since $\sinh\zeta > \zeta$. On the other hand, the $Q_{\mathrm{EDL}}(\tau)$ exhibits more pronounced nonmonotonic charging behavior, when nonlinear PNP theory is used. In addition, the nonmonotonicity is more pronounced when the EDL is driven further away from equilibrium, namely, when U_{M} is more negative, for the SBOC, see FIG 2(a). The same phenomenon exists for $Q_{\mathrm{M}}(\tau)$ in FIG S3.

Is this nonmonotonic charging dynamics unique for the nonlinear PNP theory? No, we observe nonmonotonic charging dynamics when L is reduced below $0.52\lambda_D$ (5 nm for the present case) even for the linear PNP theory, as shown in FIG 2(b). This indicates that the nonmonotonic charging dynamics is caused not by nonlinearity but by nanoconfinement. To interpret this nonmonotonicity of the charging curve, we track the time evolution of the net charge density ($\rho = C_+ - C_-$) for the linear PNP theory at $L = 0.52\lambda_D$, $U_{\mathrm{M}} = -20$ in FIG S5. We notice that, when $\tau \leq 3.8$, the curve of $\rho{\sim}X$ is elevated with increasing time, indicating that counterions are attracted to the electrode surface to form the diffuse layer (*48*). When $\tau > 3.8$, the curve of $\rho{\sim}X$ gradually decays because the surface charge is already overscreened by the counterions, thus the excess amount of counterions need to be balanced by coions in the diffuse later. Therefore, the net charge density decreases until equilibrium is reached (*11*). In summary, the proposed model reveals overscreening phenomenon in SBOCs induced by nanoconfinement.

The nonlinear and nonmonotonic effects depend on two key parameters, L and U_{M}. Herein, we introduce two related descriptors, $\varDelta_{\mathrm{nlin}}$ and $\varDelta_{\mathrm{nmon}}$,

$$\varDelta_{\mathrm{nlin}} = \frac{Q_{\mathrm{nlin}} - Q_{\mathrm{lin}}}{Q_{\mathrm{lin}}}, \tag{13}$$

which is the relative difference of Q_{EDL} between nonlinear PNP and linear PNP, and,

$$\varDelta_{\mathrm{nmon}} = \frac{Q_{\mathrm{max}} - Q_{\mathrm{eq}}}{Q_{\mathrm{eq}}}, \tag{14}$$

which is the relative difference of Q_{EDL} between maximum and equilibrium values. Both ratios are functions of U_{M} and L, as shown in FIG 2 (c-d). In FIG 2 (c), we calculate $\varDelta_{\mathrm{nlin}}$ at a dimensionless time $\tau = 2$, because the nonlinear effect is most pronounced in this range. Δ_{nlin} is larger at small L and large $|U_{\mathrm{M}}|$, and Δ_{nlin} is greater than 1 when $L < 5.4\lambda_D$ (52 nm) and $|U_{\mathrm{M}}| > 6.1$ (0.15 V), namely, when the electric field $E > 30\,\mathrm{kV/cm}$. The electric field in the SEI has been estimated to be about $> 50\,\mathrm{kV/cm}$, using nonlinear conductivity spectroscopy (*23, 49*). Therefore, nonlinear PNP theory is more accurate to describe ion transport in this case. In FIG 2 (d), Δ_{nmon} is greater than 0.2 when $L < 1.4\lambda_D$ (13 nm) and $|U_{\mathrm{M}}| > 12.5$ (0.31 V), suggesting that nonmonotonic dynamic charging is more pronounced under such conditions. In other words, nonmonotonic charging behavior is enhanced in nanoconfinement with a higher electric field.

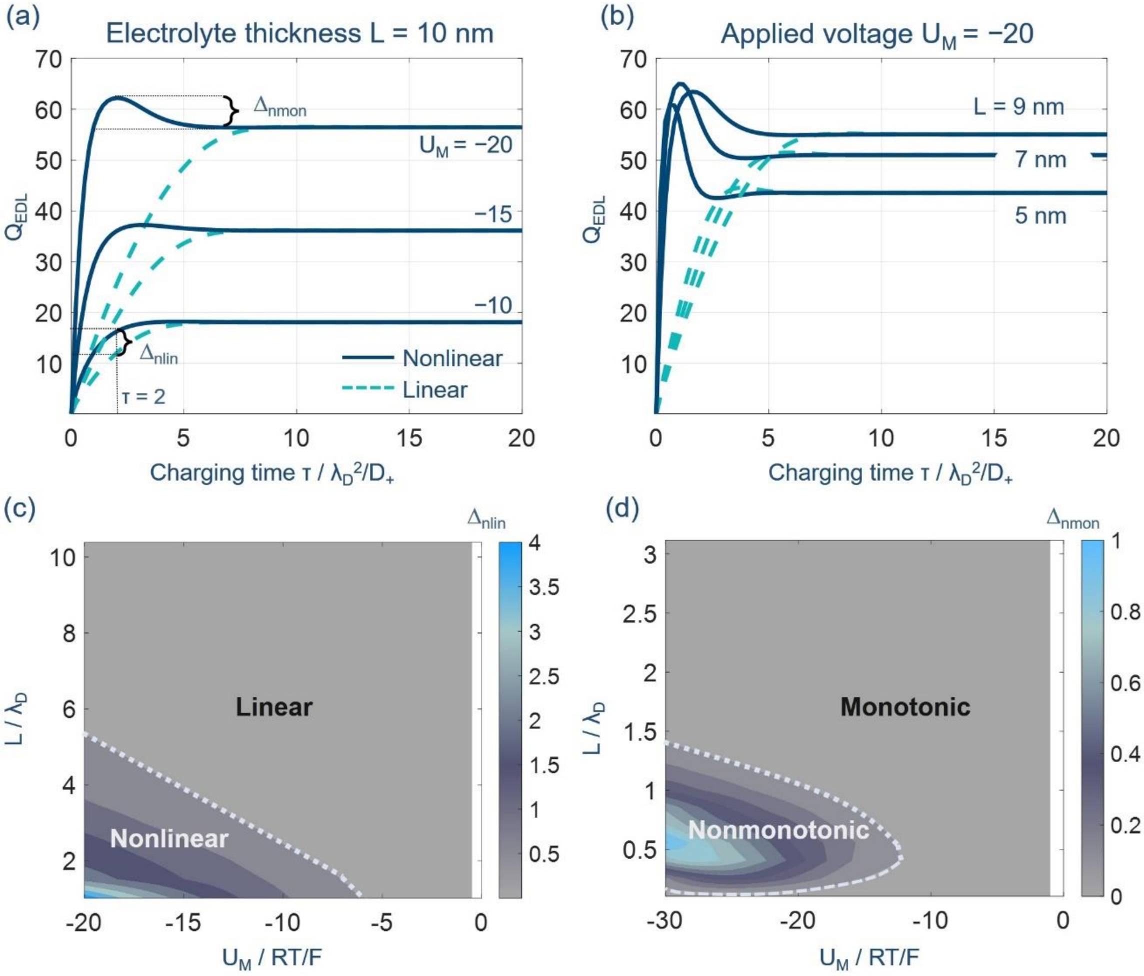

FIG 2. The charging dynamics of nanoconfined electrolytes in terms of the total diffuse charge $Q_{\mathrm{EDL}}(\tau)$ for the nonlinear (line) and linear PNP theory (dash line) at (a) different applied voltages and (b) electrolyte thicknesses for the single-blocking open cells. (c) Regime of nonlinearity of the PNP theory. (d) Regime of nonmonotonic EDL charging

dynamics. Model parameters are $c_0 = 1 \times 10^{-3}\,\mathrm{mol\,L^{-1}}, D_\pm = 1 \times 10^{-11}\,\mathrm{m^2\,s^{-1}}, \delta_{\mathrm{HP}} = 0.3\,\mathrm{nm}$, and the corresponding references values are $\lambda_D \approx 9.63\,\mathrm{nm}, t_{ref} = {\lambda_D}^2/D_+ = 9.27 \times 10^{-7}\,\mathrm{s}, U_{ref} = RT/F = 25\,\mathrm{mV}$.

Electrochemical impedance spectroscopy (EIS) allows analyzing ion transport in a wide frequency range. The EIS response for SBOC and DBCC are solved analytically at PZC (*50, 51*), see technical details in supplementary note 5, and numerically at other potentials following the method of Refs.(*52, 53*). There is no difference between the linear PNP theory and nonlinear PNP theory in the EIS response because the sinusoidal potential is a small perturbation signal, see FIG S7. Contrary to the time-domain results, EIS calculated from two definitions of EDL charge are nontrivially different. In this section, we describe the EIS response of the SBOC, and provide the results of the DBCC in FIG S8.

At the PZC, namely, $U_{\mathrm{M}}^{\mathrm{dc}} = 0$, the impedance based on Q_{EDL} is analytically expressed as,

$$Z_{\mathrm{EDL}} = \frac{1}{j\omega C_{\mathrm{H}}} \frac{\lambda_1}{1 - \mathrm{sech}\left(\sqrt{\lambda_1} L/\lambda_D\right)} + \frac{1}{j\omega C_{\mathrm{GC}}^{0}} \frac{\dfrac{\tanh\left(\sqrt{\lambda_1} L/\lambda_D\right)}{\sqrt{\lambda_1}} + \dfrac{L}{\lambda_D}(\lambda_1 - 1)}{1 - \mathrm{sech}\left(\sqrt{\lambda_1} L/\lambda_D\right)}, \tag{15}$$

where C_{H} is the Helmholtz capacitance, $C_{\mathrm{H}} = \frac{\epsilon_{\mathrm{HP}}}{\delta_{\mathrm{HP}}}$, C_{GC}^{0} the Gouy-Chapman capacitance at PZC, $C_{\mathrm{GC}}^{0} = \frac{\epsilon_{\mathrm{s}}}{\lambda_D}$, and $\lambda_1 = 1 + j\omega \frac{\lambda_D^2}{D_+}$. With asymptotical analysis provided in supplementary note 5, in the low frequency range, Eq. ((15) is asymptotic to

$$Z_{\mathrm{EDL}} = \frac{1}{j\omega}\left(\frac{1}{C_{\mathrm{H}}} + \frac{1}{C_{\mathrm{GC}}^{0}}\right), \tag{16}$$

a capacitive behavior corresponding to the equilibrium EDL capacitance. In the high frequency range, Eq. ((15) is asymptotic to,

$$Z_{\mathrm{EDL}} = \frac{\lambda_D^2}{C_{\mathrm{H}} D_+} + \frac{\lambda_D L}{C_{\mathrm{GC}}^{0} D_+} \approx \frac{L}{\dfrac{2F^2 c_0 D_+}{RT}} = \frac{L}{\sigma_s}, \tag{17}$$

a pure resistance behavior, where $\sigma_{\mathrm{s}} = \frac{2F^2 c_0 D_+}{RT}$ is the electrical conductivity of the bulk electrolyte.

The impedance response from Q_{M} at the PZC is analytically obtained as,

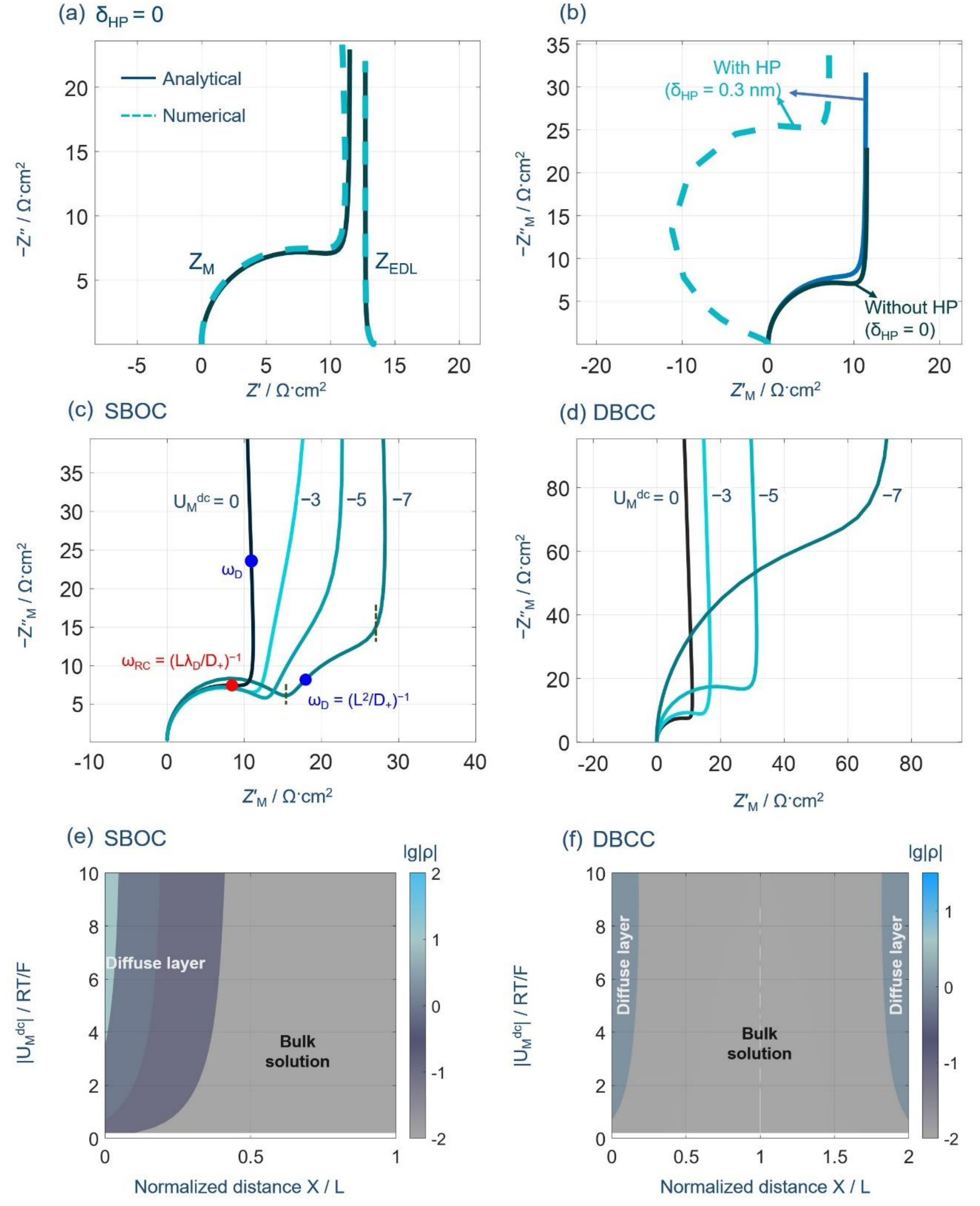

FIG 3. EIS of ion transport in the single-blocking open cells. (a) Comparison between the EIS calculated from the total diffuse charge, denoted as Z_{EDL}, and that from the

electrode surface charge, Z_{M}, at the potential of zero charge, $U_{\mathrm{M}}^{\mathrm{dc}}=0$, $\delta_{\mathrm{HP}}=0\,\mathrm{nm}$. Analytical and numerical results are displayed as solid and dashed lines, respectively. (b) Influence of the Helmholtz plane (HP) on analytical (solid lines) and numerical (dashed lines) solutions of Z_{M}. Z_{M} at different electrode potentials $U_{\mathrm{M}}^{\mathrm{dc}}$ for the (c) SBOC and (d) the DBCC at $L=100\,\mathrm{nm}$, $\delta_{\mathrm{HP}}=0\,\mathrm{nm}$. (e-f) Distribution of the net charge density at different $U_{\mathrm{M}}^{\mathrm{dc}}$'s for the SBOC and the DBCC, respectively. Model parameters are $c_0=1\times10^{-3}\,\mathrm{mol\,L^{-1}}$, $D_{\pm}=1\times10^{-11}\,\mathrm{m^2\,s^{-1}}$, $E_{\mathrm{M}}=2.5\times10^{-3}\sin\omega t\quad\mathrm{V}$, $E_{\mathrm{eq}}=E_{\mathrm{pzc}}=0$. Frequency range is $1\times10^{6}\sim1\times10^{-1}$ Hz.

$$Z_{\mathrm{M}}=\frac{1}{j\omega C_{\mathrm{H}}}+\frac{1}{j\omega C_{\mathrm{GC}}^{0}}\frac{\dfrac{\tanh\left(\sqrt{\lambda_1}L/\lambda_D\right)}{\sqrt{\lambda_1}}+\dfrac{L}{\lambda_D}(\lambda_1-1)}{\lambda_1},\tag{18}$$

In the low frequency range, Eq. ((18) asymptotically approaches,

$$Z_{\mathrm{M}}=\frac{1}{j\omega}\left(\frac{1}{C_{\mathrm{H}}}+\frac{1}{C_{\mathrm{GC}}^{0}}\right),\tag{19}$$

which is the same as Z_{EDL} in the low frequency range. In the high frequency range, Eq. ((18) approaches,

$$Z_{\mathrm{M}}=\frac{1}{\dfrac{C_{\mathrm{GC}}^{0}D_{+}}{\lambda_D L}+j\omega\dfrac{\epsilon_{\mathrm{s}}}{L}}=\frac{1}{\dfrac{1}{R_{\mathrm{ele}}^{\mathrm{pzc}}}+j\omega C_{\mathrm{geo}}},\tag{20}$$

where $R_{\mathrm{ele}}^{\mathrm{pzc}}=\frac{\lambda_D L}{C_{\mathrm{GC}}^{0}D_{+}}=\frac{L}{\sigma_{\mathrm{s}}}$ is the electrolyte resistance at the PZC and $C_{\mathrm{geo}}=\frac{\epsilon_{\mathrm{s}}}{L}$ the geometric capacitance of the electrolyte.

In contrast to a pure resistor given by Z_{EDL}, a semicircle is expected in the high frequency range for Z_{M}. Consistent with above theoretical analysis, the EIS calculated based on Q_{EDL} shows a nearly vertical line, the EIS calculated based on Q_{M} shows a semicircle in high frequency range followed by a vertical line in low frequency range, see FIG 3 (a). The agreement between analytical and numerical results at $\delta_{\mathrm{HP}}=0$ confirms the accuracy of the numerical method when the HP is not considered. In FIG 3 (b), the influence of the HP on analytical and numerical solutions at the PZC is examined. The existence of the HP brings about an anomalous semicircle in the second quadrant for the numerical results in the dashed line. This anomalous feature is a numerical artifact because it disappears in the analytical results in the solid line. Neglecting the HP, we find the numerical results are converged to the analytical results, and the mere difference is in the length of the low-frequency vertical line, which is readily understood as the change of the EDL capacitance, *c.f.*, Eq.(19). Hence, we neglect the HP effects in subsequent effects since our focus is put on the high-frequency semicircle.

When the potential deviates from the PZC, namely, $U_{\mathrm{M}}^{\mathrm{dc}} \neq 0$, a newly tilted line can be observed in the intermediate frequency of Z_{M} in FIG 3 (c). This can be attributed to the finite-rate ion transport in the inhomogeneous electrolyte featuring a time scale of $\tau_D = (\omega_D)^{-1} = L^2/D_+$, leading to the frequency dispersion of the double-layer capacitance. This frequency-dispersion phenomenon is only observed in the SBOC, not in the DBCC of which the EIS is given in FIG 3 (d). The reason is that the diffuse layer is more pronounced in the SBOC than in the DBCC when $U_{\mathrm{M}}^{\mathrm{dc}} \neq 0$, as shown in FIG 3 (e-f). Ion transport in the whole of the electrolyte features a time constant of $\tau_{RC} = (\omega_{RC})^{-1} = \lambda_D L/D_+$.

Katayama et al. measured the EIS of Ni/LiPON/Li at several electrode potentials (*54*). The Nyquist plots show a semicircle in the high-frequency range, followed by a nearly vertical line; they found that the diameter of the semi-circle derived from the LiPON thin film increases with increasing electrode potential, consistent with the trend of Z_{M} of DBCC in FIG 3 (d). The potential dependence of the impedance of Ni/LiPON/Li is reproduced in FIG 4 (a). FIG 4 (b) shows the dependence of the electrolyte resistance, R_{ele}, defined as $R_{\mathrm{ele}} = Z_{\mathrm{M}}'(\omega \to 0)$, of the DBCC on electric potential $U_{\mathrm{M}}^{\mathrm{dc}}$. The model-based result in FIG 4 (b) is calculated using the parameters from ref.(*37, 54, 55*), where $c_0 = 0.25\ \mathrm{M}$, $D_+ = 2 \times 10^{-12}\ \mathrm{m}^2\ \mathrm{s}^{-1}$, $\epsilon_{\mathrm{s}} = \epsilon_{\mathrm{LiPON}} = 16.6\varepsilon_0$, $2L = 760\ \mathrm{nm}$. Increasing the applied potential, the electrolyte resistance R_{LiPON} increases gradually due to the decreasing ion concentration at the middle plane, $C_{+,\mathrm{mid}}^{\mathrm{eq}}$, as shown in FIG 4 (c-d). To save the calculation time, we calculate $C_{+,\mathrm{mid}}^{\mathrm{eq}}$ using $2L = 200$ nm. Since $C_{+,\mathrm{mid}}^{\mathrm{eq}}$ is uniformly distributed, increasing the electrolyte thickness to 760 nm will not affect the results. The steady-state cation concentration $C_{+,\mathrm{mid}}^{\mathrm{eq}}$ is decreased at more negative $U_{\mathrm{M}}^{\mathrm{dc}}$. The relationship between $C_{\mathrm{mid}}^{\mathrm{eq}}$ and $U_{\mathrm{M}}^{\mathrm{dc}}$ can be described by an approximate analytical expression originally given in ref.(*56*),

$$C_{\mathrm{mid}}^{\mathrm{eq}} = \mathrm{A} - \sqrt{\mathrm{A}^2 - 1}, \tag{21}$$

where,

$$\mathrm{A} = 1 + 8\left(\frac{\lambda_D}{L}\right)^2 \left[\sinh\left(\frac{U_{\mathrm{M}}^{\mathrm{dc}}}{4}\right)\right]^4. \tag{22}$$

FIG 4 (d) indicates that the analytical solution captures numerical results. Experimental values are overall larger than model-based values, which could be attributed to the surface roughness of the metal electrode (*32, 33, 57*).

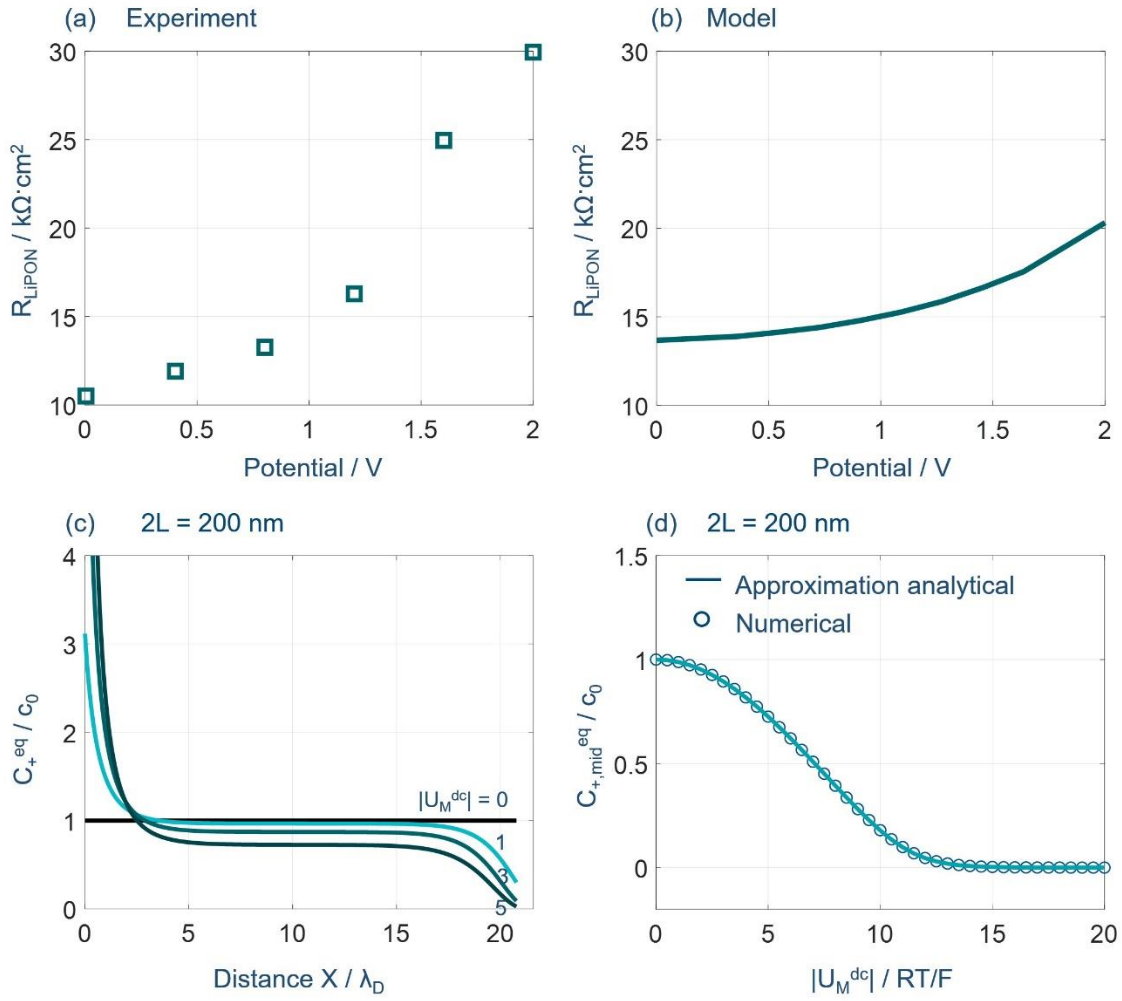

FIG 4. EIS of ion transport in the double-blocking closed cells. (a-b) Comparison between model and experimental results of the EIS response at different potentials. Experimental data were reported by Katayama et al. in Ni/LiPON/Li(*54*). The model-based result is calculated using $c_0 = 0.25\,\mathrm{M}$, $D_+ = 2 \times 10^{-12}\,\mathrm{m^2\,s^{-1}}$, $\epsilon_s = 16.6\varepsilon_0$, $2L = 760\,\mathrm{nm}$. (c) shows the steady-state distribution of cation concentration at different applied voltages, and (d) the steady-state cation concentration at the middle plane as a function of applied voltage. Analytical and numerical results are displayed as solid and dashed lines, respectively. Model parameters are $c_0 = 1 \times 10^{-3}\,\mathrm{mol\,L^{-1}}$, $D_\pm = 1 \times 10^{-11}\,\mathrm{m^2\,s^{-1}}$, $2L = 200\,\mathrm{nm}$, $\delta_{\mathrm{HP}} = 0\,\mathrm{nm}$.

So far our analysis has been focused on blocking electrodes. As practical situations usually involve reactive, non-blocking electrodes, one may wonder if the insights collected on the blocking electrodes also apply for non-blocking electrodes. This question is briefly touched upon below.

Specifically, two more cases involving non-blocking electrodes are considered, including a single reactive open cell with the left side in contact with a non-blocking electrode and the right side connected to a reservoir of electrolyte solution, and a single blocking closed cell with the left side in contact with a blocking electrode, and the right side connected to a non-blocking electrode (see supplementary notes 5 and 9).

For the case of single reactive open cell, the nonlinear and nonmonotonic effects are also observed, and the quantitative difference is that $Q_{\mathrm{EDL}}(\tau)$ decreases at larger rate constant $k_{0,ct}$. This is because the metal deposition reaction consumes cations, thus lowering Q_{EDL}. The regimes of nonlinearity of the PNP theory and nonmonotonic EDL charging dynamics are basically the same as for the case of SBOC. Therefore, we conclude that the main conclusions previously drawn for the single blocking open cell also applicable to a reactive electrode. For the case of single blocking closed cell, we notice that the EIS consists of two semicircles in high- and intermediate-frequency range and a vertical line in low-frequency range. With increasing rate constant $k_{0,ct}$, the intermediate-frequency semicircle associated with the charging transfer decreases. The high-frequency semicircle corresponds to the electrolyte resistance in parallel with the geometric capacitance, and a vertical line in low frequency range corresponds to the equilibrium EDL capacitance. Therefore, a nonblocking metal on the right side will bring forth a new semicircle attributed to the charging transfer reaction in the intermediate-frequency range.

In summary, nonlinear-PNP theory has been employed to describe ion transport in nanoconfined electrolytes in single-blocking open cell (SBOC) and double-blocking closed cell (DBCC) configurations. The SBOC shows a surprising nonmonotonic double-layer charging behavior. When the EDL charge refers to the total ionic charge in the diffuse layer, the EIS shows a nearly vertical line. When the EDL charge refers to the electrode surface charge, the EIS shows a semicircle in the high-frequency range and a vertical line in the low-frequency range. An additional impedance arc in the moderate to low frequency range is observed only for the SBOC at potentials deviating from the potential of zero charge. The high-frequency semicircle represents the electrolyte resistance in parallel with the geometric capacitance of the electrolyte. The tilted line at intermediate-frequency represents the ion transport in the inhomogeneous electrolyte, leading to the frequency dispersion of the double-layer capacitance. The low-frequency vertical line is associated with the equilibrium double-layer capacitance. Experimental data of ion transport in solid electrolyte are interpreted using the DBCC model. We also briefly discussed the influence of charge transfer reactions on the results. For the case of single reactive open cell, the time-domain charging dynamic behaviors are qualitatively the same as in the SBOC case. In frequency space, a non-blocking metal on the right side will bring forth a new semicircle attributed to the charging transfer reaction in the intermediate frequency range. A more detailed analysis of reactive, non-blocking electrodes will be reported in future.

Associated content

The Supporting Information is available free of charge via the internet at http://pubs.acs.org.”

Comparison between Q_{EDL} and Q_{M} in time space; Double layer charging dynamics in terms of Q_{M} for the SBOC; Comparison of Q_{EDL} between the DBCC and the SBOC; Time evolution of net charge density distribution in the SBOC; Double layer charging dynamics in terms of Q_{EDL} for the single reactive open cell; Analytical solution of EIS at PZC; Comparison of EIS between linear PNP and nonlinear PNP theory for the SBOC; EIS response of the DBCC; EIS response of the Single blocking closed cell.

Acknowledgment

This work is supported by the Initiative and Networking Fund of the Helmholtz Association (No. VH-NG-1709).

Reference

1. G. Schmidt, M. Suermann, B. Bensmann, R. Hanke-Rauschenbach, I. Neuweiler, Modeling Overpotentials Related to Mass Transport Through Porous Transport Layers of PEM Water Electrolysis Cells. *Journal of The Electrochemical Society* **167**, 114511 (2020).
2. M. K. Zhang *et al.*, Bell shape vs volcano shape pH dependent kinetics of the electrochemical oxidation of formic acid and formate, intrinsic kinetics or local pH shift? *Electrochimica Acta* **363**, 137160 (2020).
3. M. K. Zhang *et al.*, How Buffers Resist Electrochemical Reaction-Induced pH Shift under a Rotating Disk Electrode Configuration. *Anal Chem* **93**, 1976-1983 (2021).
4. J. Gonzalez, E. Guillen, E. Laborda, A. Molina, Quantitative analysis of the electrochemical performance of multi-redox molecular electrocatalysts. A mechanistic study of chlorate electrocatalytic reduction in presence of a molybdenium polyoxometalate. *Journal of Catalysis* **413**, 467-477 (2022).
5. Bard A. J., Faulkner L. R., White H. S., *Electrochemical methods: Fundamentals and applications*. John Wiley & Sond, vol. 38 (2002).
6. M. Z. Bazant, K. Thornton, A. Ajdari, Diffuse-charge dynamics in electrochemical systems. *Phys Rev E* **70**, 021506 (2004).
7. D. Yan, M. Z. Bazant, P. M. Biesheuvel, M. C. Pugh, F. P. Dawson, Theory of linear sweep voltammetry with diffuse charge: Unsupported electrolytes, thin films, and leaky membranes. *Phys Rev E* **95**, 033303 (2017).
8. C. Lin, R. G. Compton, Understanding mass transport influenced electrocatalysis at the nanoscale via numerical simulation. *Current Opinion in Electrochemistry* **14**, 186-199 (2019).
9. M. Z. Bazant, M. S. Kilic, B. D. Storey, A. Ajdari, Towards an understanding of induced-charge electrokinetics at large applied voltages in concentrated solutions. *Advances in colloid and interface science* **152**, 48-88 (2009).
10. M. V. Fedorov, A. A. Kornyshev, Towards understanding the structure and capacitance of electrical double layer in ionic liquids. *Electrochimica Acta* **53**, 6835-6840 (2008).
11. M. Z. Bazant, B. D. Storey, A. A. Kornyshev, Double layer in ionic liquids: overscreening versus crowding. *Phys Rev Lett* **106**, 046102 (2011).
12. J. Jiang, D. Cao, D.-e. Jiang, J. Wu, Kinetic charging inversion in ionic liquid electric double layers. *The journal of physical chemistry letters* **5**, 2195-2200 (2014).
13. A. A. Lee, S. Kondrat, D. Vella, A. Goriely, Dynamics of Ion Transport in Ionic Liquids. *Phys Rev Lett* **115**, 106101 (2015).
14. A. A. Lee, D. Vella, S. Perkin, A. Goriely, Are Room-Temperature Ionic Liquids Dilute Electrolytes? *J Phys Chem Lett* **6**, 159-163 (2015).
15. A. Yochelis, Spatial Structure of Electrical Diffuse Layers in Highly Concentrated Electrolytes: A Modified Poisson–Nernst–Planck Approach. *The Journal of Physical Chemistry C* **118**, 5716-5724 (2014).
16. K. Ma, M. Janssen, C. Lian, R. van Roij, Dynamic density functional theory for the charging of electric double layer capacitors. *J Chem Phys* **156**, 084101 (2022).
17. M. te Vrugt, H. Löwen, R. Wittkowski, Classical dynamical density functional theory: from fundamentals to applications. *Advances in Physics* **69**, 121-247 (2020).

18. C. Lian, S. Zhao, H. Liu, J. Wu, Time-dependent density functional theory for the charging kinetics of electric double layer containing room-temperature ionic liquids. *J Chem Phys* **145**, 204707 (2016).

19. Z. Zhang, Y. Gao, S. Chen, J. Huang, Understanding Dynamics of Electrochemical Double Layers via a Modified Concentrated Solution Theory. *Journal of The Electrochemical Society* **167**, 013519 (2019).

20. Y. Gao *et al.*, Ion-vacancy coupled charge transfer model for ion transport in concentrated solutions. *Science China Chemistry* **62**, 515-520 (2019).

21. I. Riess, J. Maier, Symmetrized general hopping current equation. *Phys Rev Lett* **100**, 205901 (2008).

22. L. Zhang, J. Cai, Y. Chen, J. Huang, Modelling electrocatalytic reactions with a concerted treatment of multistep electron transfer kinetics and local reaction conditions. *J Phys Condens Matter* **33**, 504002 (2021).

23. B. Roling, L. N. Patro, O. Burghaus, M. Gräf, Nonlinear ion transport in liquid and solid electrolytes. *The European Physical Journal Special Topics* **226**, 3095-3112 (2017).

24. A. Heuer, S. Murugavel, B. Roling, Nonlinear ionic conductivity of thin solid electrolyte samples: Comparison between theory and experiment. *Physical Review B* **72**, 174304 (2005).

25. I. Riess, J. Maier, Current Equation for Hopping Ions on a Lattice under High Driving Force and Nondilute Concentration. *Journal of The Electrochemical Society* **156**, P7 (2009).

26. T. Asano, Y. Kaneko, A. Omote, H. Adachi, E. Fujii, Conductivity Modulation of Gold Thin Film at Room Temperature via All-Solid-State Electric-Double-Layer Gating Accelerated by Nonlinear Ionic Transport. *ACS Appl Mater Interfaces* **9**, 5056-5061 (2017).

27. F. Wieland, A. P. Sokolov, R. Bohmer, C. Gainaru, Transient Nonlinear Response of Dynamically Decoupled Ionic Conductors. *Phys Rev Lett* **121**, 064503 (2018).

28. L. Benitez, J. M. Seminario, Ion Diffusivity through the Solid Electrolyte Interphase in Lithium-Ion Batteries. *Journal of The Electrochemical Society* **164**, E3159-E3170 (2017).

29. R. Guo, B. M. Gallant, Li2O Solid Electrolyte Interphase: Probing Transport Properties at the Chemical Potential of Lithium. *Chemistry of Materials* **32**, 5525-5533 (2020).

30. N. Kaiser, S. Bradler, C. König, B. Roling, In Situ Investigation of Mixed Ionic and Electronic Transport across Dense Lithium Peroxide Films. *Journal of The Electrochemical Society* **164**, A744-A749 (2017).

31. E. Gongadze, U. van Rienen, V. Kralj-Iglic, A. Iglic, Spatial variation of permittivity of an electrolyte solution in contact with a charged metal surface: a mini review. *Comput Methods Biomech Biomed Engin* **16**, 463-480 (2013).

32. P. Lu, C. Li, E. W. Schneider, S. J. Harris, Chemistry, Impedance, and Morphology Evolution in Solid Electrolyte Interphase Films during Formation in Lithium Ion Batteries. *The Journal of Physical Chemistry C* **118**, 896-903 (2014).

33. Y. Li, K. Leung, Y. Qi, Computational Exploration of the Li-Electrode|Electrolyte Interface in the Presence of a Nanometer Thick Solid-Electrolyte Interphase Layer. *Acc Chem Res* **49**, 2363-2370 (2016).

34. A. Wang, S. Kadam, H. Li, S. Shi, Y. Qi, Review on modeling of the anode solid electrolyte interphase (SEI) for lithium-ion batteries. *npj Computational Materials* **4**, 15 (2018).

35. Y. Iriyama, T. Kako, C. Yada, T. Abe, Z. Ogumi, Charge transfer reaction at the lithium phosphorus oxynitride glass electrolyte/lithium cobalt oxide thin film interface. *Solid State Ionics* **176**, 2371-2376 (2005).

36. L. O. Valøen, J. N. Reimers, Transport Properties of $LiPF_6$-Based Li-Ion Battery Electrolytes. *Journal of The Electrochemical Society* **152**, A882 (2005).

37. L. Le Van-Jodin, F. Ducroquet, F. Sabary, I. Chevalier, Dielectric properties, conductivity and Li+ ion motion in LiPON thin films. *Solid State Ionics* **253**, 151-156 (2013).

38. Z. M. Zhang, Y. Gao, S. L. Chen, J. Huang, Understanding dynamics of electrochemical double layers via a modified concentrated solution theory. *Journal of The Electrochemical Society* **167**, 013519 (2020).

39. J. H. C.-K. Li, Impedance response of electrochemical adsorption. *J. Phys. Condens. Matter* **33**, 164003 (2021).

40. J. Huang, On obtaining double-layer capacitance and potential of zero charge from voltammetry. *Journal of Electroanalytical Chemistry* **870**, 114243 (2020).

41. J. Jiang, D. Cao, D. E. Jiang, J. Wu, Kinetic Charging Inversion in Ionic Liquid Electric Double Layers. *J Phys Chem Lett* **5**, 2195-2200 (2014).

42. A. R. Duarte, F. Batalioto, G. Barbero, A. M. Neto, Electric impedance of a sample of dielectric liquid containing two groups of ions limited by ohmic electrodes: a study with pure water. *J Phys Chem B* **117**, 2985-2991 (2013).

43. Z. Guo, X. Ren, L. Li, R. He, Y. Gao, Hierarchical Porous Electrode Impedance Model Based on Diffusion Dynamics and the Electrode Morphology and Prediction of Electric Double-Layer Structures. *ACS Applied Energy Materials* **6**, 508–518 (2022).

44. J. Wu, Understanding the Electric Double-Layer Structure, Capacitance, and Charging Dynamics. *Chem Rev* **122**, 10821-10859 (2022).

45. J. Cheng *et al.*, A Theoretical Model for the Charging Dynamics of Associating Ionic Liquids. *Frontiers in Chemical Engineering* **4**, 23 (2022).

46. J. R. MaCdonald, Double Layer Capacitance and Relaxation in Electrolytes. *Trans. Faraday Soc.* **66**, 943–958, (1970).

47. A. A. KORNVSHEV, Conductivity and space charge phenomena in solid electrolytes with one mobile charge carrier species, a review with original material. *Electrochimica Acta* **26**, 303-323 (1981).

48. A. A. Kornyshev, Double-layer in ionic liquids: paradigm change? *J Phys Chem B* **111**, 5545-5557 (2007).

49. S. Murugavel, B. Roling, Application of nonlinear conductivity spectroscopy to ion transport in solid electrolytes. *Journal of Non-Crystalline Solids* **351**, 2819-2824 (2005).

50. C. K. Li, J. Huang, Impedance Response of Electrochemical Interfaces: Part I. Exact Analytical Expressions for Ideally Polarizable Electrodes. *Journal of The Electrochemical Society* **167**, 166517 (2021).

51. C. Li, J. Zhang, J. Huang, Impedance response of electrochemical interfaces. Ⅲ, Fingerprints of couplings between interfacial electron transfer reaction and electrolyte-phase ion transport. *The Journal of Chemical Physics* **157**, 18 (2022).

52. D. Klotz, M. Schönleber, J. P. Schmidt, E. Ivers-Tiffée, New approach for the calculation of impedance spectra out of time domain data. *Electrochimica Acta* **56**, 8763-8769 (2011).

53. C.-K. L. Lu-Lu Zhang, Jun Huang, A Beginners' Guide to Modelling of Electric Double Layer under Equilibrium, Nonequilibrium and AC Conditions. *J. Electrochem.* **28**, 2108471 (2022).

54. R. Furuya, N. Serizawa, Y. Katayama, Potential Dependence of the Impedance of Solid Electrolyte Interphase in Some Electrolytes. *Electrochemistry* **90**, 057002-057002 (2022).

55. R. Furuya, N. Tachikawa, K. Yoshii, Y. Katayama, T. Miura, Deposition and Dissolution of Lithium through Lithium Phosphorus Oxynitride Thin Film in Some Ionic Liquids. *Journal of The Electrochemical Society* **162**, H634-H637 (2015).

56. J. J. Lopez-Garcia, J. Horno, C. Grosse, Impedance-Frequency Response of Closed Electrolytic Cells. *Micromachines (Basel)* **14**, 368 (2023).

57. H. Ekström, G. Lindbergh, A Model for Predicting Capacity Fade due to SEI Formation in a Commercial Graphite/LiFePO4Cell. *Journal of The Electrochemical Society* **162**, A1003-A1007 (2015).

TOC